CoCr alloy processed by Selective Laser Melting (SLM): effect of Laser Energy Density on microstructure, surface morphology, and hardness

Lavinia Tonelli, Alessandro Fortunato, Lorella Ceschini

CoCr alloy processed by Selective Laser Melting (SLM): effect of Laser Energy Density on microstructure, surface morphology, and hardness.

In: Journal of Manufacturing Processes 52 (2020) 106–119

CoCr alloy processed by Selective Laser Melting (SLM): effect of Laser Energy Density on microstructure, surface morphology, and hardness.

Lavinia Tonelli[1], Alessandro Fortunato[1], Lorella Ceschini[2]*

[1] Department of Industrial Engineering (DIN), Alma Mater Studiorum - University of Bologna, Viale Risorgimento 2, 40136 Bologna (Italy)

[2] Department of Civil, Chemical, Environmental and Materials Engineering (DICAM), Alma Mater Studiorum - University of Bologna, Viale Risorgimento 2, 40136 Bologna (Italy)

***corresponding author:** lavinia.tonelli2@unibo.it, lavinia.tonelli@gmail.com
Department of Industrial Engineering – University of Bologna
Viale Risorgimento 4, 40136 Bologna (Italy)
Tel +39 0512093465 Fax +39 0512093467

Abstract

Selective Laser Melting (SLM) was used to realize Co-28Cr-6Mo samples. Several process parameters were considered, resulting in a wide range of Laser Energy Density (LED). The study was focused on the investigation of both process and material-related aspects, such as surface morphology, laser tracks dimension and defects formation mechanisms. In addition, macro (HRC) and microhardness ($HV_{0.5}$) was assessed. A correlation between LED value and density, surface quality, microstructural features and hardness of SLM parts was defined. The final goal was to identify, for the biomedical Co-28Cr-6Mo alloy, the optimal LED window to be considered in order to maximize the overall quality of SLM parts.

Keywords

Selective Laser Melting (SLM); Additive Manufacturing (AM); Laser Beam Melting (LBM); Biomaterial; Co-based alloys; Co28Cr6Mo

Highlights

- Co28Cr6Mo SLM samples built with Laser Energy Density (LED) from 43 to 268 J mm^{-3}
- In-depth characterization of top and lateral surfaces
- Comprehensive examination of microstructural defects resulting from SLM
- LED well correlated to surface quality, microstructural features and hardness
- Optimized range for high quality Co28Cr6Mo SLM parts: LED=150-200 J mm^{-3}

1. Introduction

Selective Laser Melting (SLM) is a one of the most widespread and studied Additive Manufacturing (AM) technology for metallic materials, belonging to the Powder Bed Fusion (PBF) process that enables the fabrication of 3D parts by melting a bed of fine metallic powders layer-by-layer using a laser beam [1–4]. The base of the SLM process is the STL (Standard Triangulation Language) model of the final part, that can afford a high level of complexity. The model is virtually sliced in thin layers (thickness 0.02-0.04 mm), then every layer of powder undergoes melting by means of a computer-guided laser beam. The process continues by melting powders layer by layer, the consolidation between two consecutive layers occurs on account of the Rayleigh length of the incoming beam and conduction heating [5,6]. SLM is a quite complex technology driven by several process parameters, including: thickness of the layer of powders, laser power, scanning strategy and velocity, chamber atmosphere, support structures, building direction, to name the most important ones [6]. When producing parts through an AM technique, the first target is to obtain near-full-density components, since it is well known that high porosity content is detrimental for mechanical properties. In this regard, process parameters play an important role and must be optimized in order to return defect-free pieces with high mechanical properties. It is well-established that four major parameters, such as

laser power P [W], scanning velocity v [mm s^{-1}], distance between two consequent laser scans h [mm] and layer thickness d [mm] can be combined in the Laser Energy Density (LED), also named volume energy, by the formula $LED = P/(v \cdot h \cdot d)$ [J mm^{-3}] [5]. As demonstrated by recent publications, LED is directly related to some of the features involved in the densification process such as density, porosity content and defect formation mechanism [7–10]. In addition, a critical aspect of the SLM technology relies in the high roughness of the as-built surfaces that can be also related to the process parameters [6]. In this view, the determination of the critical LED range, capable to return overall high-quality parts, is crucial. Presently, SLM technology has been successfully applied to a number of metallic materials including Fe-based [11–13], Ni-based [14–16], and Al-based [17–20] alloys. The benefits that AM can bring to the biomedical field has already been illustrated in the literature [4,21,22]. Fisrtly, they allow an affordable customization to make the device fit the patient anatomy. In addition, for the specific case of Ti and Co-based alloys, AM process enable to overcome the limits imposed by the conventional manufacturing routes [23,24]. Among metallic biomaterials, CoCrMo alloys are widely used for the production of medical devices like dental and orthopedic implants in account of their long-term corrosion resistance, high wear resistance and mechanical strength [25]. Several studies have been carried out on CoCrMo alloys processed with SLM to realize such medical devices [26–33]. However, most of these studies focus on the technological and mechanical aspects of the SLM of CoCrMo and a comprehensive analysis of the effect of different process parameters on the surface quality, microstructure and properties of the final components is currently lacking. Hence, the aim of the present study was to correlate LED to surface quality of the as-build components, microstructure and hardness. A number of CoCrMo samples have been processed via SLM setting various process parameters in order to obtain a wide range of LED values, then a full microstructural investigation was carried out, along with the characterization of surface morphology and macro and micro hardness tests. The final purpose was to identify major process-related features (including material discontinuities) and to define an optimized LED interval.

2. Materials and methods

2.1 SLM samples production

Gas atomized CoCrMo powder, provided by LPW Technology (LPW Technology Ltd, Runcorn, UK) were used for SLM samples production. They were nominally spherical in shape and with size ranging from 15 to 45 μm. Their nominal chemical composition (wt.%) given by the supplier is reported in Table 1 and complies with the requirements of the ASTM F75 standard (Co-28Cr-6Mo casting alloy) [34].

Table 1: Chemical composition (wt.%) of CoCr powders used for the production of samples given by LPW supplier, compared with requirements according to ASTM F75 standard (Co-28Cr-6Mo casting alloy).

	Co	**Cr**	**Mo**	**Si**	**Mn**	**Fe**	**Ni**	**C**	**W**	**Ti**	**O**
LPW	Bal.	27.00 – 30.00	5.00 – 7.00	< 1.00	< 1.00	< 0.75	0.25 – 0.50	< 0.16	< 0.20	< 0.10	< 0.10
ASTM F75	Bal.	27.00 – 30.00	5.00 – 7.00	< 1.00	< 1.00	< 1.00	< 0.50	< 0.35	< 0.20	< 0.10	-

Samples in form of parallelepiped (20 x 6 x 30 mm^3) were realized using the SLM equipment SISMA MYSINT100 provided with an Yb-fiber laser (λ = 1070 nm), with a maximum power of 200 W and a nominal focused spot diameter of 50 μm. Samples were built in a nitrogen atmosphere with a low residual content of oxygen (0.3 vol%). Process parameters and scanning strategy were settled using MARCAM AutoFab software. A wide range of process parameters, reported in Table 2, were considered, in order to obtain several LED values. Scanning strategy of each layer was designed as a chessboard: the layer is divided in 3x3 mm blocks then the laser beam scans each block following parallel lines whose direction is perpendicular to the one of the adjacent blocks. Every next layer, the chessboard pattern is rotated by 45°. Building direction of samples was unique and perpendicular to the base plate.

Table 2: Process parameters used for the production of samples, leading to different values of $LED = P/(v \cdot h \cdot d)$.

P [W]	***v [mm s^{-1}]***	***h [mm]***	***d [mm]***	***LED [J mm^{-3}]***
70; 90; 110; 130; 150	500; 700; 900; 1100	0.04; 0.06; 0.08	0.02; 0.03	43.21 - 267.86

2.2 Powders characterization

Shape, morphology and chemical composition of powders were characterized by a Scanning Electron Microscope equipped with an Energy Dispersive X-ray Spectroscope (SEM-EDS, Zeiss EVO 50). The presence of internal porosity was assessed with Optical Microscopy (OM, Zeiss Imager A1) and SEM analyses of powders cross sections.

2.3 SLM Parts Characterization

In order to assess the surface quality of SLM parts, both lateral and top surfaces, as represented in Fig.1, were characterized by SEM-EDS analyses and surface roughness was evaluated with a stylus profilometer (Hommelwerke T2000, 5 µm tip radius). The density of all SLM samples was determined following Archimedes' principle; at least three measurements were performed on each sample using an analytical balance (precision ± 0.0001 g). With respect to the building direction, the microstructural characterization was carried out both on longitudinal (L) and transverse (T) cross-sections, as shown in Fig.1. Prior to the microstructural characterization, standard metallographic techniques were used for samples preparation, including mechanical grinding (with 180–2500 grit SiC papers) and polishing up to 1µm diamond suspension. In order to reveal the microstructure, electrochemical etching was performed at 4 V for 20 s, in a solution of hydrochloric acid and ferric chloride dissolved in distilled water (5 mL HCl, 10 g $FeCl_3$, 100 mL H_2O) [35]. OM and SEM-EDS analyses were accomplished on both L and T samples produced under a wide range of LED values. With the aim to correlate the process parameters, in terms of LED, and the resulting microstructure,

a number of measurements (such as porosity evaluation and estimation of laser tracks) were carried out using the ImageJ software for image analysis on both OM and SEM micrographs. Phase composition of samples produced with high, medium and low LED was determined by X-Ray Diffraction (PANalytical Expert PRO with Xcelerator detector) provided with a Cu-Kα radiation source (λ = 0.15405 nm) and carrying out θ - 2θ scans from 30° to 100° with a 0.017° step size and a 15 s dwell time, performed at 40 kV and 40 mA. Hardness of the SLM parts were evaluated both by Rockwell (HRC) and Vickers (HV0.5, 10 s dwell time) tests.

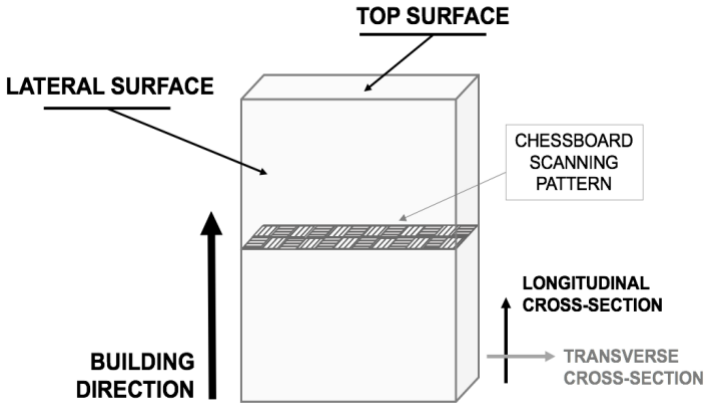

Figure 1: Scheme reporting, with respect to a SLM part, surfaces considered for morphological investigations (Top and Lateral) and direction for metallographic samples extraction (Longitudinal and Transverse).

3. Results and Discussion

3.1 Characterization of the powders

Representative SEM micrographs of free powders (Fig.2a,b) show that they were mainly spherical in shape even if satellites and collapsed particles were also detected on the surface of powders, making powders morphology uneven. In the high magnification SEM image (Fig.2b) it is also possible to observe the dendritic phase, as highlighted by arrows. Dendritic phase is distinctive of the feedstock powders since SLM components, on the contrary, solidify with a cellular microstructure [36]. The chemical composition was investigated by SEM-EDS analyses on free powders and the results

matched the standard of ASTM F75 and composition given by the supplier. As reported by Hebert [37] and Sames et al. [38], gas trapped in the feedstock powders might negatively influence the quality of the final parts, leading to the formation of bubbles in the melt pool. In this view, powders cross-sections were analyzed and, as reported in Fig.2c, no internal porosities were detected.

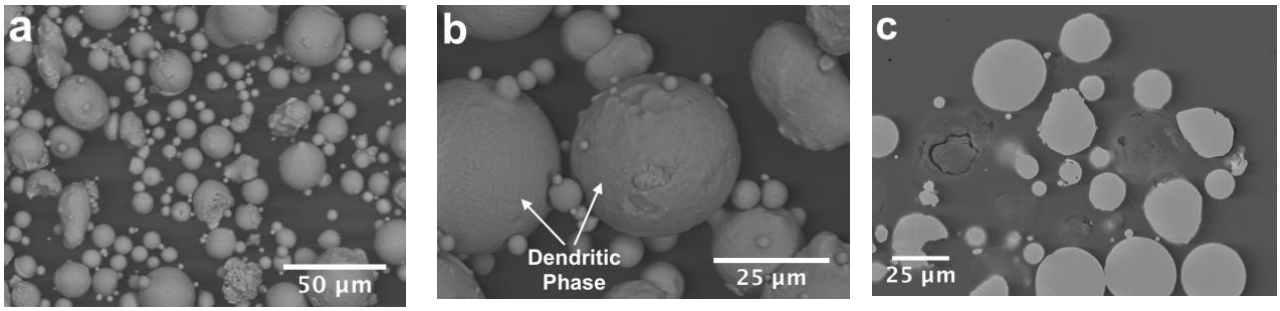

Figure 2: SEM micrographs: low (a) and high (b) magnification of free powders, (c) powders cross-section.

It is worth mentioning that on few cases it was possible to identify powders with an anomalous morphology, due to the presence of round darker regions. The particle represented in Fig.3 shows an almost perfect spherical shape and a smooth surface, dendritic phase is clearly recognizable but darker areas can be also detected on particle surface. SEM-EDS analyses, also reported in Fig.3, suggest the existence, in correspondence of darker areas, of oxides with a higher content of Si and Mn and the presence of Al and Ca, while the chemical composition of dendritic phases still complies with data reported in Tab.1.

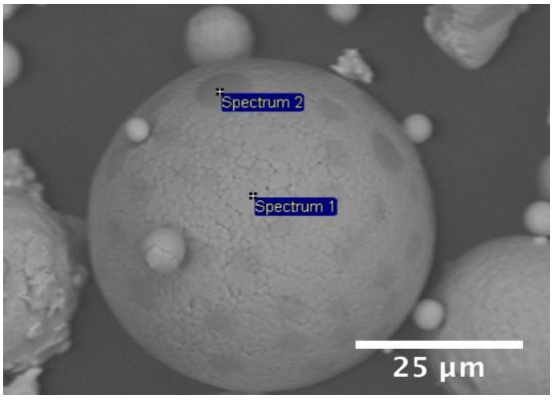

	O	Al	Si	Ca	Cr	Mn	Co	Mo
Spectrum 1	2.93	-	0.99	-	28.15	0.99	61.24	5.69
Spectrum 2	30.83	1.92	12.01	0.31	25.62	11.46	16.65	1.13

Figure 3: SEM-EDS analyses performed on anomalous powder particles: chemical composition (wt.%) of dendritic phase (Spectrum 1) and darker areas (Spectrum 2).

3.2 Characterization of the SLM samples

The first assessment of the quality of SLM samples regarded the measurement of the density. The nominal density value of a Co-28Cr-6Mo component produced by conventional investment casting, is 8.3 g cm^{-3}, as reported in ASTM F75 [34]. Density measurements were carried out following the well-known Archimedes' method, repeating the measurement at least three times for each SLM sample. For the same alloy produced by additive manufacturing, this method has been proved to be quite accurate even if compared with more sophisticated technology [39]. The results of density measurements on the SLM parts as a function of LED are reported in Fig.4, where the nominal density of the conventional Co-28Cr-6Mo casting alloy is reported as well (dotted line). From the results of density measurements, it is possible to define a critical value of LED (100 J mm^{-3}) beyond which samples produced by SLM exhibit a density comparable to a conventional casting component. In few cases, the measured density was even higher than the reference one, due to the superficial roughness of SLM component and open porosities on the surface that may compromise the correct determination of the weight of the sample immersed in water. So, in order to verify the correspondence of density

measurements with porosity of SLM parts, the actual area occupied by internal porosities was measured on polished cross-sections of selected samples using the ImageJ software for image analysis and results are still reported in Fig.4. By increasing the LED, internal porosity content decreases reaching the minimum percentage (approximately 0.1) for value of LED higher than 150 J mm^{-3}. Therefore, even if a LED value beyond 100 J mm^{-3} is sufficient to obtain parts with a density comparable to the conventional one, in order to obtain a sound component with an extremely low porosity content, such value has to be equal to or higher than 150 J mm^{-3}.

In the reason of these previous results and with the aim to better highlight the relationship between microstructural features and process parameters, the SLM samples have been separated in three different classes, according to the LED applied during the process: low (up to 100 J mm^{-3}), medium (100-150 J mm^{-3}) and high (150-270 J mm^{-3}) LED class. A total of 30 samples were produced in the current study, distributed as follows: 15 for the low, 10 for the medium and 5 for the high LED class. Low LED results in inadequate density and high porosity content, so in a poor quality of SLM parts. Medium LED returns a porosity percentage less than 1, while high LED values lead to almost defect-free components.

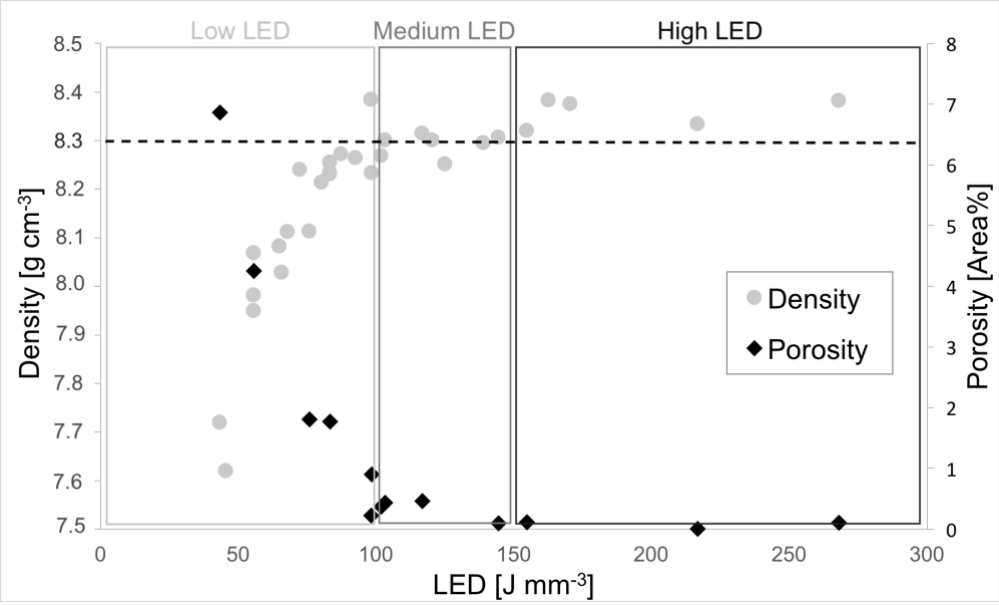

Figure 4: Density and internal porosity of SLM samples as a function of LED, measured by Archimedes' method and image analysis on polished cross sections, respectively. Dotted line defines the reference value of a conventional cast component (8.3 g cm^{-3}) while frames define ranges of low, medium and high LED.

3.2.1 Assessment of surface quality

An important feature of SLM components is represented by surface quality and part of the recent literature has been focused on classifying the proper methodologies to perform surface metrology of AM products [40]. It is well known, in fact, that this technology generates high surface roughness and, generally, SLM parts need post-process finishing. With the aim to investigate the relationship between energy density and surface quality, the lateral and top surfaces of samples were characterized in the as-built conditions. Qualitative SEM analyses of the morphology of lateral surfaces, reported in Fig.5, showed no remarkable differences between sample processed with low, medium or high LED. Lateral surfaces are mainly characterized by sintered or semi-molten powders, clearly identifiable by the dendritic phase, as well by porosities (as shown by the cross-section in Fig.6).

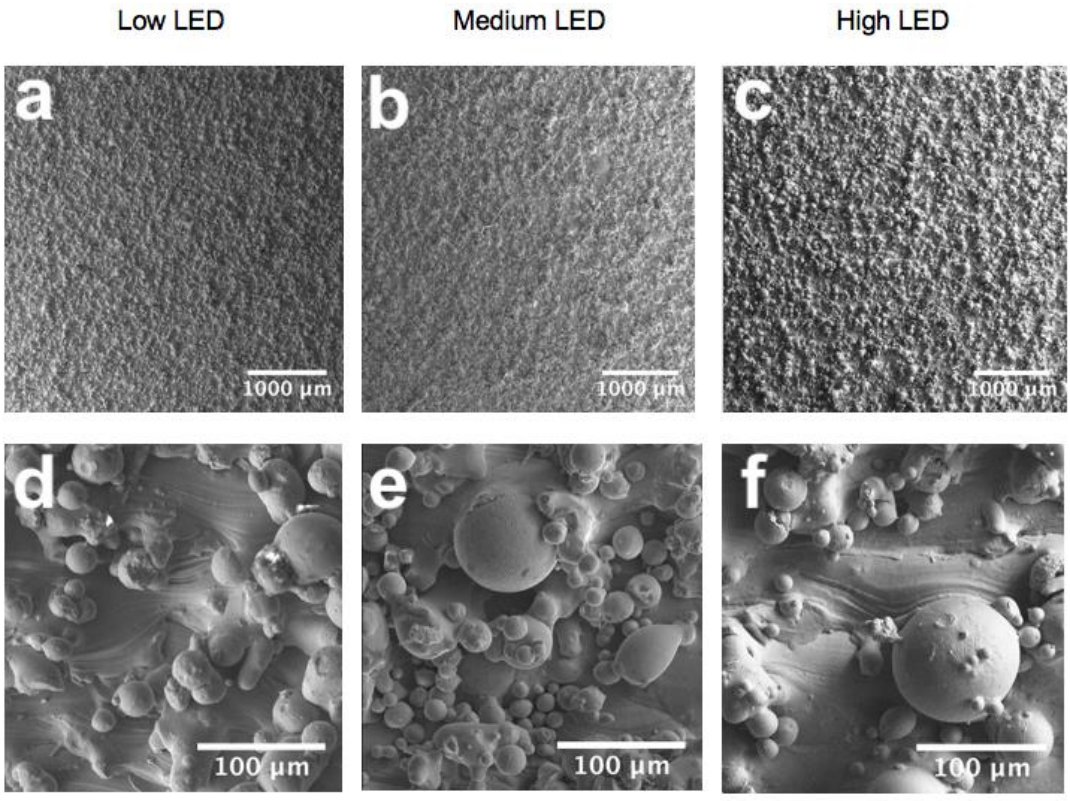

Figure 5: Low and high magnification SEM micrographs on lateral surface of representative samples processed with: (a) and (d) Low LED, (b) and (e) Medium LED, (c) and (f) High LED.

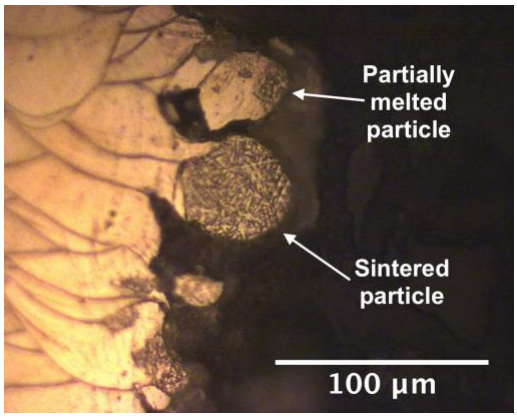

Figure 6: Optical Micrograph of a polished cross-section of a representative lateral surface.

Profilometric measurements, summarized in in Fig.7, confirmed the results of SEM analyses: they returned values of average surface roughness in the range Ra=8-12 µm and they are not directly related to LED. On the basis of these outcomes, it appears that stochastic phenomena, in terms of powders distribution in the layer, dominate the resulting roughness of lateral surfaces (in direct contact with the powder bed).

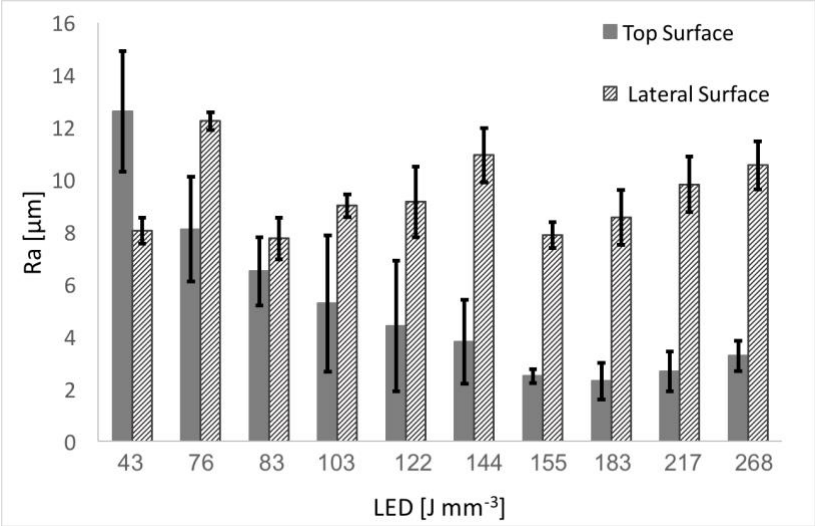

Figure 7: Average surface Roughness (Ra) measured on both lateral and top surface on samples with increasing LED values.

The roughness of the top surface, instead, is strongly dependent on LED: a low energy applied on the powder bed leads to high roughness (max Ra=13 µm), while increasing LED leads to smoother surfaces, reaching the lowest roughness (Ra=2.5-3 µm) in case of samples produced with high LED (over 150 J mm^{-3}). The observation of top surfaces with the aid of SEM (Fig.8) allowed to explain

the profilometric results: while for medium and high LED (Fig.8d,f) the chessboard scanning pattern in easily recognizable and laser scans are even and regular, in case of low LED (Fig.8a) the resulting surface is irregular, with discontinuous scans and cavities. High magnification micrographs of medium and high LED samples (Fig.8e,g) show regular and narrowed laser scans, representing the solidified elongated molten pools with an analogue morphology for both samples, already observed by Zhou et al. [41]. It is worth mentioning that top surfaces of the as-built samples represent a single layer of melted and solidified powders, consequently the analysis and observation of these surfaces are fundamental in order to appreciate melt pool dynamics and principal related aspects. Another important factor regarding surface quality is related to the deposition of the following layer of powders: a smooth surface, in fact, will improve flowability of particles, on the contrary a rough one might lead to an uneven distribution of powders with an evident downside on the quality of the final part. As already illustrated by other authors [42,43], the discontinuous and chaotic morphology showed by low LED samples is the result of an unstable melt flow that leads to the incomplete wetting and spreading of the molten material during the process. Therefore, irregularities can be ascribed to defects of material filling or localized lacks of fusion, as well as spatter ejection of molten material from the pool, bringing to cavities and coarseness showed in Fig.8b. As a consequence, porosities and partially melted powder particles can be easily detected on the surface of low LED samples, as represented in Fig.8c. Recent works [44–46] analyzed the dynamics of fluid and particles during laser powder bed fusion, highlighting that spatter ejection and denudation are phenomena strictly related to this technology and dependent on process parameters. The denudation is defined as a depleting of powders in the regions surrounding laser tracks [47] while spatter ejection is promoted by the so-called laser-induced plume. The laser plume tends to eject molten material away from the liquid pool and particles ejected from the liquid pool solidify before falling down on the powders bed and, by reacting with the residual oxygen in the chamber atmosphere, they may change their chemical composition [44]. The stability of the molten pool is dominated by the balance between spatter ejection due to the laser plume and Marangoni convection, that tends to spread molten material from

the center of the melt pool to the outer regions [45]. Since the direction of the plume and its temperature are mainly dependent on scanning velocity and pattern and laser power, so on LED, a careful optimization of these parameters must be performed [46]. The relation between energy input and spatter ejection has been also investigated by Wang et al. [44] for a CoCrMoW dental alloy, showing that raising the energy input leads to increase spattering. While in samples processed with low LED the molten pool was clearly unstable leading to a disarranged top surface, in samples processed with medium and high LED the morphology of the top surface is even and regular and only a few discontinuities on the laser pattern can be observed (Fig.8d,e). Two kinds of defects were detected on the surface of medium and high LED samples: spattering and Marangoni flow related phenomena, represented in Fig.8h. Spattering appears as fully re-melted spherical particles that have been reincorporated in the layer. Marangoni flow is, instead, related to the local changes of surface tensions that affects the stability of the melt pool, so the proper wetting and spreading of the liquid. Oxygen content, in particular, plays an important role on local changes of surface tension by dramatically reducing it; reduction in the surface tension reverses the direction of the Marangoni flow, leading to the formation of large globular islands, as already observed in the SLM of tungsten [42].

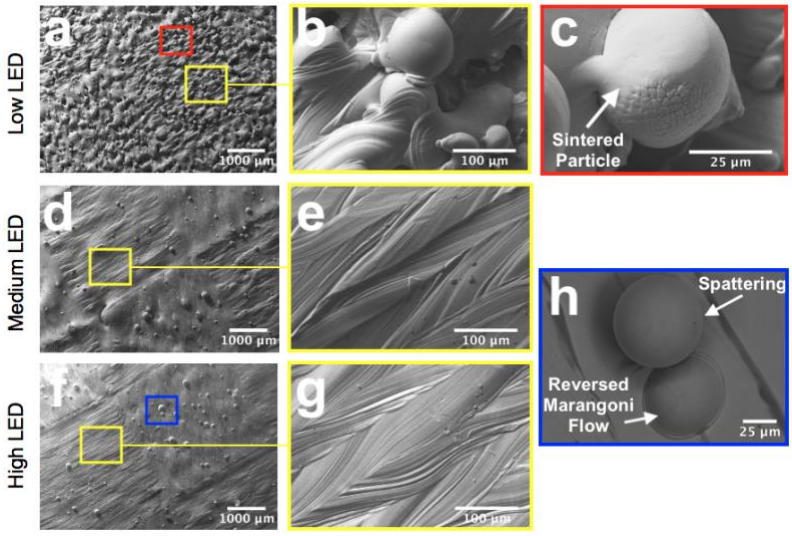

Figure 8: SEM analyses on top surface: (a), (d), (f) low magnification of low, medium and high LED samples; (b), (e), (g) details of area defined by yellow frames of low, medium and high LED samples, (c) details of area defined by red frame showing a sintered particle on low LED samples, (h) details of area defined by blue frame showing spattering and Marangoni related defects on high LED samples.

Cross-sections analyses of the main defects observed on the top surfaces are reported in Fig.9: sintered particles (Fig.9a) are defined by the dendritic phase as previously observed in the feedstock powders; spattering defects (Fig.9b) shows no dendritic phase, proving that material underwent melting and then rapidly solidified into a spherical shape; reversed Marangoni phenomena are clearly characterized by a centripetal, instead of a centrifugal, flow that moved the molten material from the outside into the center of the pool.

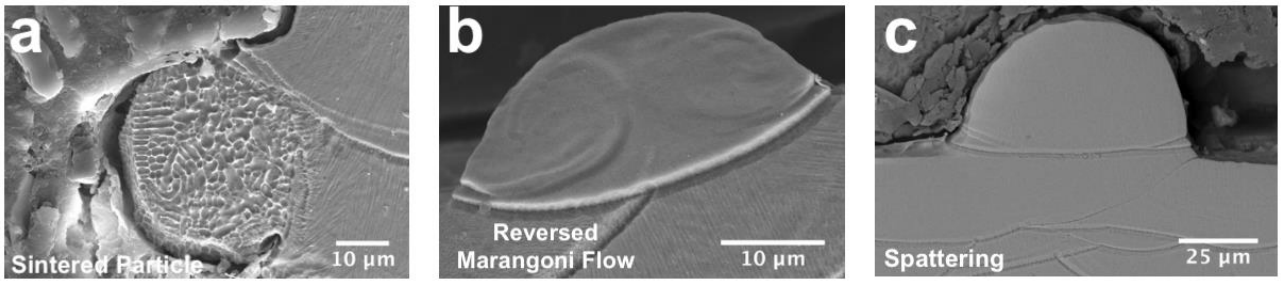

Figure 9: SEM micrographs of representative defects detected on top surfaces: (a) sintered particle on low LED samples, (b) reversed Marangoni flow and spattering defects on medium and high LED samples.

SEM-EDS analyses were performed on regular solidified tracks in order to verify the presence of a local segregations; results show that darker area in Fig.10 (corresponding to the center and outer region of the melt pool) exhibit higher Si and Mn content (wt.%), with also a not negligible content of oxygen, Al and Mg, in particular located at the center of the track. Similar outcomes have been previously reported in the case of feedstock powders and, presumably, the two phenomena are related. It is possible that Al-O-Si compounds derive from the feedstock powder and, during solidification of the melted powder bed, high melting compounds are ejected into the liquid phase and segregation can occur in the reason of the spreading of liquid phase driven by Marangoni flow from the center to the outer of the melt pool [36,45].

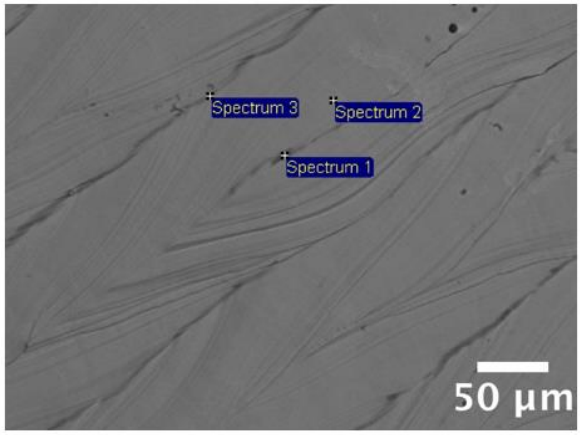

	O	Mg	Al	Si	Cr	Mn	Co	Mo
Spectrum 1	28.63	0.21	0.69	8.14	23.58	6.43	29.89	2.43
Spectrum 2	-	-	-	0.87	28.24	1.13	63.13	6.63
Spectrum 3	1.66	-	-	1.12	28.28	1.22	61.07	6.38

Figure 10: SEM-EDS analyses performed on a laser track on the top surface: micrograph showing the investigated regions and relative chemical composition (wt.%).

3.2.2 Macro-level microstructural features

It is well known that SLM parts are characterized by a hierarchical microstructure that can be divided in macro-level and micro-level microstructural features. Material discontinuities (i.e. defects) and texture fall within the first category, while morphology and size of grains and phase composition fall in the second one [48]. Next sections report on these macro and micro-level microstructural features. Representative micrographs of T and L cross-sections of samples produced with different LED levels are illustrated in Fig.11, they clearly prove that process parameters, in terms of applied energy, have a noticeable influence on the final microstructure. Low LED values (Fig.11a,d) lead to a chaotic microstructure, with a large extent of internal porosity and lacks of fusion, while medium (Fig.11b,e) and high values of LED (Fig.11c,f) lead to a more regular and continuous microstructure, with a negligible presence of porosities, as previously reported. On transverse cross-sections, the pattern resulting from the chessboard scanning strategy of each layer can be clearly identified, since laser

tracks appear well highlighted by the etching. Longitudinal cross-sections, instead, evidence the melt pool overlap, due the highly localized melting of powder.

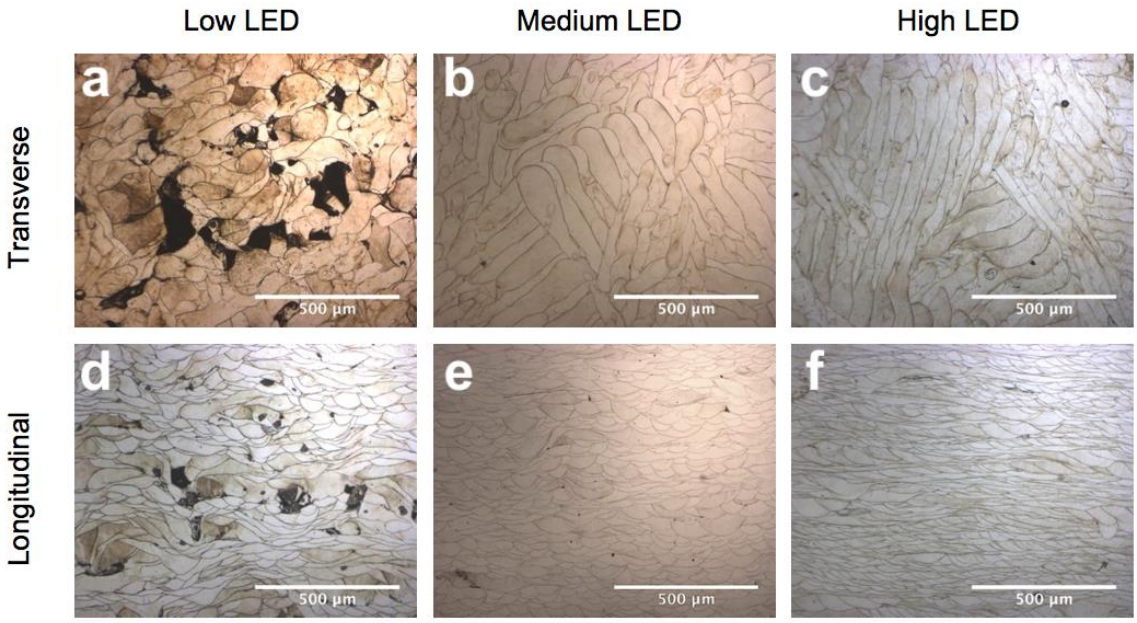

Figure 11: Low magnification optical micrographs of transverse and longitudinal cross sections samples produced with low (a) and (d), medium (b) and (e) and high (c) and (f) LED. Layer thickness was 0.03 mm for low LED sample and 0.02 mm for the medium and high ones.

On sound components, exhibiting an even microstructure and few solidification defects, a number of microstructural analyses were carried out: the width of the tracks left by the subsequent passages of the laser was evaluated on T-sections and an attempt to estimate the mean size of the residual melt pool area was carried out on L ones. In order to obtain a reliable value of the laser track widths, a total of 54 different measurements for each sample, distributed in different region of the T section, were accomplished and the results are showed in Fig.12. According to the manufacturer, the nominal spot diameter for the SLM machine used in this experiment is 50 µm and the majority of the investigated samples exhibited residual tracks wider than 50 µm, thus indicating that the actual volume of material involved in the melting process is wider than the one directly affected by the beam, on account of heat conduction.

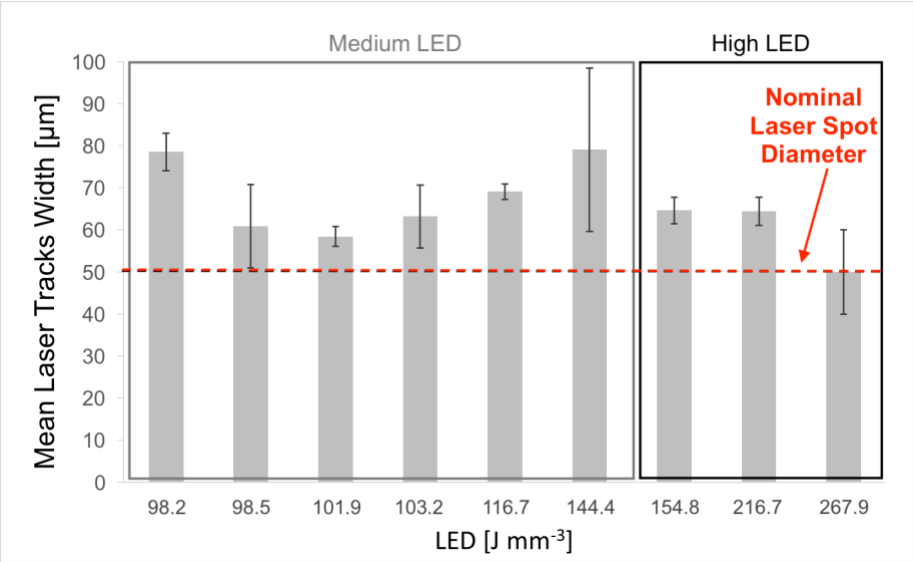

Figure 12: Mean laser tracks widths measured on transverse cross-section of samples with increasing LED, the red dashed line defines the reference value of the nominal laser spot diameter.

The dimensions of the residual mean melt pool area was estimated by adapting conventional procedures for the evaluation of the average grain size described in the ASTM E112-12 standard [49]. The analysis was carried out with the aim to evaluate the average dimension of the residual melt pool area resulting from the whole SLM process, that involves re-melting due to the processing of subsequent layers and complex scanning strategy, as the chessboard pattern rotated by 45° every next layer. Two methods were considered, based on the lineal and on the circular intercept procedure, being the first usually recommended for equiaxed grains and the latter suitable for deformed grains. The average dimension of the residual melt pool area was obtained by merely dividing the length of the intercepts for the number of crossed melt pools: a total of 9 different regions for each sample in the L section were investigated. The two methods returned comparable values for the average dimension of residual melt pool area (Fig.13), ranging approximately from 25 to 35 µm. Since melt pools are almost semi-circular in shape and their sizes are related to the beam diameter (width) and layer thickness (depth) [36], it can be inferred that the measurements returned an estimation of the depth of the residual melt pool area (in this work layer thickness was set at 20 and 30 µm). The LED applied seems to have no direct connection to the extent of the residual melt pool; it is possible that, by considering the value of the energy density, the single contribution of parameters such as laser

power, layer thickness and hatch spacing was hidden. For instance, other researchers, through in-situ monitoring the melt pool dynamic and analyses of laser tracks, demonstrated that laser power has an important role in determining the size and geometry of the pool: higher laser powers lead to deeper melt pool thus impacting the aspect ratio of the melt pool [45,50].

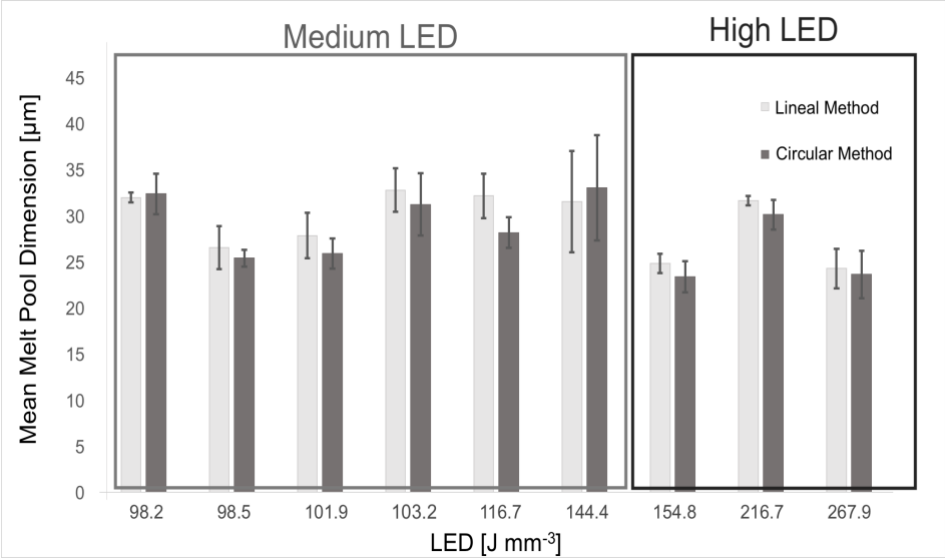

Figure 13: Average dimension of the residual melt pool area measured with both diagonal and circular method (ASTM E112-12) on longitudinal cross-section of samples with increasing LED value.

A preliminary characterization of material discontinuity (defects) can be performed by optical microscopy (Fig.14). According to Zhand et al. [51], common defects in SLM parts can be classified in three categories: cavities due to incomplete fusion, porosities and cracks. Process parameters play a key role in determining type, amount and magnitude of such defects. Incomplete melting (Fig.14a,b), also named lack of fusion, is the most common defect in samples processed with a low LED value, where the applied energy is not sufficient enough to melt the whole material and leads to an unstable molten pool, as previously discussed. Lacks of fusion may present themselves as large cavities, where un-melted powders particles can be easily recognizable by their spherical shapes and dendritic phase, as represented in Fig.14a, or as cavities, located at the bottom of a melt pool, due to poor bonding to the underlying layer, as shown in Fig.14b. A number of porosities, indicated by the yellow arrows in Fig.14a,c,d,e, can be detected on sample processed in the full range of parameters;

these defects have the typical spherical shape of gas porosities and their size is generally lower than 10 μm. In the molten pool, due to high temperature, the gas solubility in the liquid metal is elevated and, since cooling rate is extremely high, the dissolved gas might remain trapped in the solidified metal, forming the characteristic spherical porosities. Considering that feedstock powders have been previously proved to be free of internal defects (Section 3.1), such porosities might be process-related and consequent to both vaporization alloy of elements or dissolution of gas entrapped between metal powder during layer deposition. It is also possible to observe, in the L-sections of sound component, the classic Marangoni convection related phenomena, as indicated by the white arrow in Fig.14c. As formerly exposed, in the case of local changes of surface tension, the flow of molten material is reversed (from the edge of the molten pool to the center) and, once solidified, it results in a microstructural discontinuity. On sample cross-sections it is not uncommon to observed partially un-melted particles, identifiable by the dendritic structure as indicated by white arrows in Fig.14d. These defects can be found also in regular and homogenous microstructure, resulting from medium and high LED where large cavities and major lacks of fusion are not present. An example of solidification crack is represented in Fig.14e. According to [6], three types of crack can be observed in AM components: solidification cracking occurring along the solidifying layer and due to tensile stress induced by thermal contraction, liquation cracking that affects the partially melted zone and delamination. Usually, solidification cracks can be easily distinguished from poor bonding cavities, even if they are both generally located at the bottom of a solidified melt pool: the latter are surrounded by irregular melt pool with a coarser microstructure (darker area in Fig.14b), while cracks can be found in a homogeneous and regular microstructure. It worth mentioning that cracks were not very recurring in the analyzed samples, regardless of the LED value. According to Collins et al. [48], hot tearing is particularly related to high energy densities applied to the powders bed, therefore it is possible to hypothesize that the critical value of LED, beyond which hot tearing become substantial, was not reached in the present work. Finally, keyhole collapses can occur during powder bed fusion, leading to final defects similar to the one showed in Fig.14f. Keyhole melting mode was originally

studied for laser welding [52] where, for a certain combination of process parameters (i.e. laser power, speed and beam diameter), material can experience a transition in the melting mode, changing from conduction to keyhole mode. For low laser intensity (nominally lower than 10^5 MW cm^{-2}), heat transfer in the molten pool occurs by conduction; in the case of keyhole-mode the laser energy density is sufficient enough to cause partial vaporization of elements, leaving a cavity inside the liquid pool, thus allowing the laser to penetrate more deeply in the material. The same mechanism has already been observed in SLM parts [53,54]: the conduction mode lead to the formation of almost semi-circular solidified melt pool, with a ratio between depth and width of approximately 1:2; when keyhole collapse occurs, the shape is no longer semi-circular, the depth is greater and the ratio is no more respected. For the same reasons previously exposed, the gas formed by vaporization of elements can be entrapped in the solidified material, generating porosity in the final microstructure located at the end of the collapsed melt pool, as reported in Fig.14f. Keyhole formation is strongly related to the laser-powder interaction: preliminary studies demonstrated that, by increasing the time of interaction between the laser and the material, keyhole collapse is favored [45,54], thus laser speed is a relevant parameter. For a fixed time of interaction, instead, higher laser power may cause the transition from conduction to keyhole melting mode, leading to an unstable liquid pool and the formation of pore located at the bottom of the melt pool [45]. In this work it was found that keyhole phenomenon is rather limited if LED is lower than 200 J mm^{-3}.

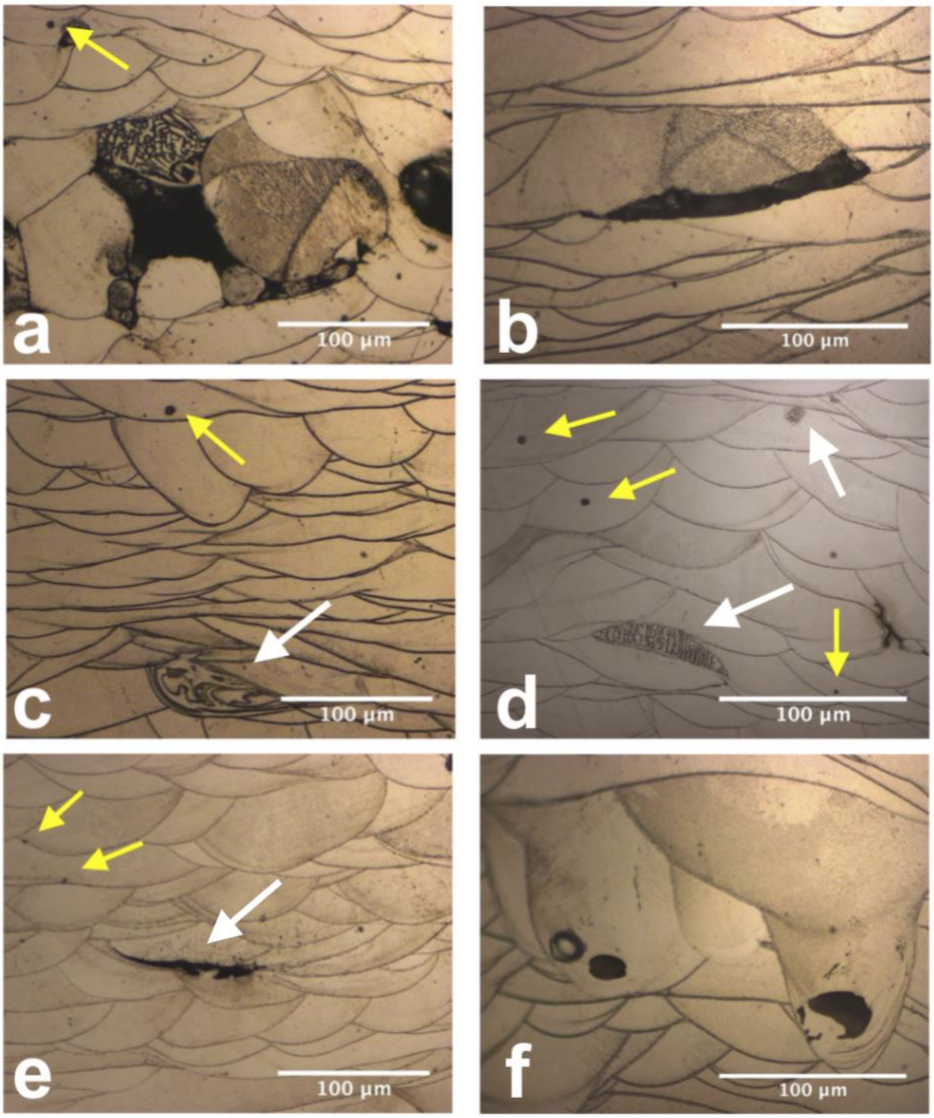

Figure 14: OM micrographs showing microstructural discontinuities found in longitudinal cross-sections of SLM parts: a) and b) lacks of fusion, c) Marangoni related phenomena (white arrow) and microporosities (yellow arrow), d) Partially un-melted particles (white arrows) and microporosities (yellow arrows), e) crack (white arrow) and microporosities (yellow arrows), f) Keyhole phenomena.

The same microstructural discontinuities were observed by SEM analyses and common defects are represented in Fig.15: lack of fusion (Fig.15a), porosity located at the bottom of the melt pool (Fig.15b), solidification cracking to the high thermal gradient (Fig.15c) and reversed Marangoni flow (Fig.15d). In the cavity, consequent of insufficient melting, the feedstock powders almost unaffected by the laser beam can be easily recognized, as well as the partially melted material and cracks propagating from the cavity to the surrounding solidified material. Gas porosity and hot tearing are usually discovered in regular and homogeneous microstructure, as showed in Fig.15b,c. Finally, when the convection flow due to Marangoni effect is reversed, the molten material solidifies in a very

chaotic and inhomogeneous microstructure (Fig.15d), where a few micro-porosities can be detected but no evidence of segregation was ascertained.

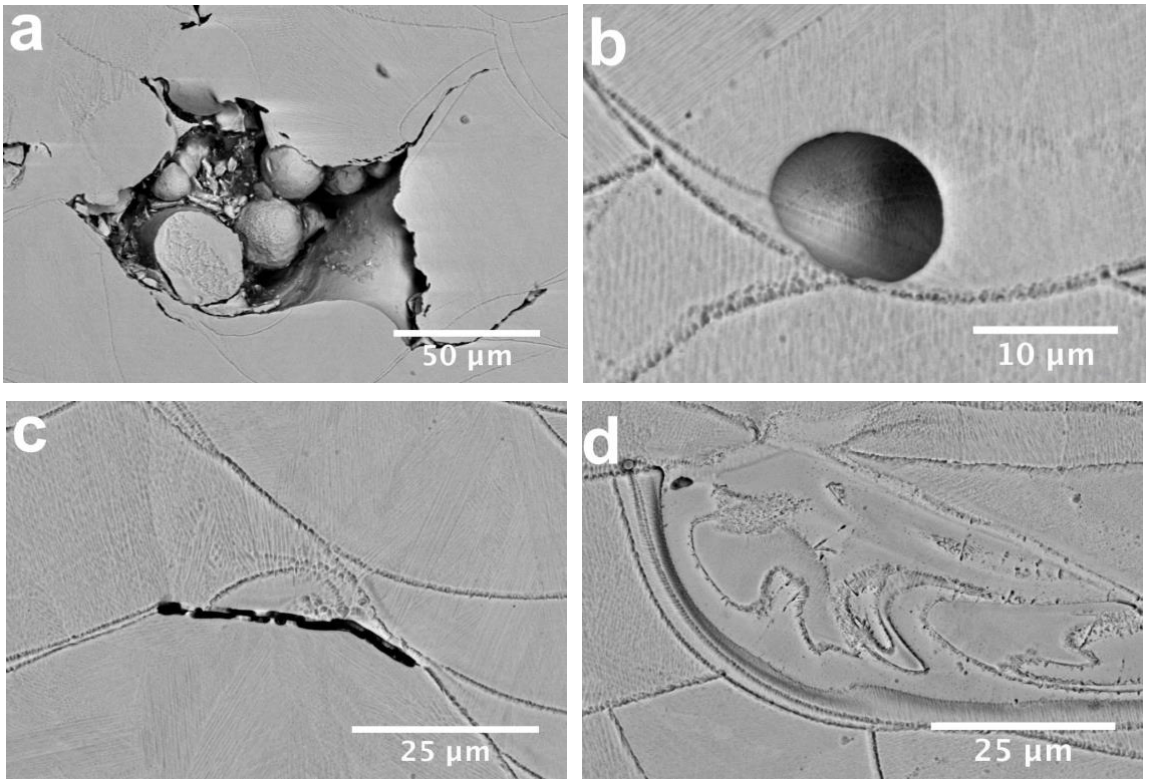

Figure 15: SEM micrographs showing discontinuities found in longitudinal cross sections of SLM parts: a) lack of fusion, b) porosity, c) crack d) Marangoni related phenomena.

On samples cross-sections a few inhomogeneities, peculiar of CoCr alloys, were detected. For instance, a Si-rich particle is represented in Fig.16a; such spherical inclusions have been already observed in the Co-28Cr-6Mo alloy processed with investment casting [55,56] and in a CoCrW dental alloy produced by casting, milling and SLM [57]. In the present study, a Si-rich film was observed also in correspondence of a crack (Fig.16b). Similar inclusions have been previously observed in the feedstock powders (Section 3.1) and on the top surfaces of SLM samples (Section 3.2.1); SEM-EDS analyses performed on such inclusions revealed, as reported before, a higher content of Si, O and Al, as observed also by Giacchi et al. [56].

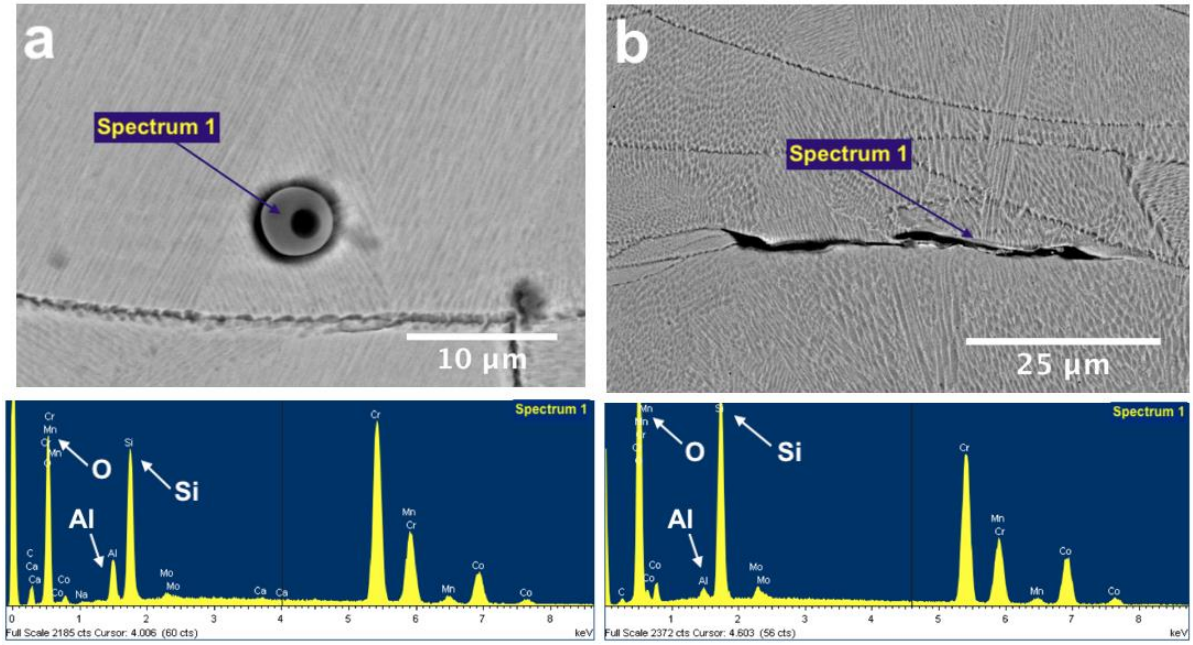

Figure 16: SEM-EDS analysis of microstructural discontinuities peculiar of CoCr alloy: a) Si-rich particle, b) crack with a Si-rich film.

Electrochemical etching of polished cross-sections and following observation under polarized light microscopy (Fig.17), revealed a texture showing preferential solidification and columnar grain growth in the direction of the highest temperature gradient, as already observed by other researchers for the same alloy [26,28,50] and generally for some metals processed by SLM [48]. In the representative optical micrographs of the L section (Fig.17c,d) it is possible to observe that columnar grain growth cross over layers, generally replicating the grain orientation of the previous layer (epitaxial growth). The epitaxial growth is governed by the heat flux and the orientation of the underlying solidified material, namely the previous processed layer. Grain growth is not oriented exactly in the same direction of the heat flux, therefore perpendicular to the layer; instead, for Co-Cr alloy [26,28] as well in the case of different metals with a cubic structure [58,59], it follows a preferential crystallographic orientation, usually one of the <100> family, close to the thermal gradient direction. However, by alternating the laser scanning direction and by rotating the scanning pattern across layers, it is possible to alternate heat flux direction resulting in a preferential <111> orientation [36,47,60]. It appears that the solidification process started in correspondence of pool boundaries and grains have grown directly from the previous layer, without changing direction. The

real-time monitoring of SLM technology applied on Ti6Al4V alloy [45] indeed demonstrated that solidification begins from boundaries of the semi-circular liquid pool and that grain growth is radial, approximately oriented along a direction comprised between the maximum local thermal gradient and the preferential growth orientation.

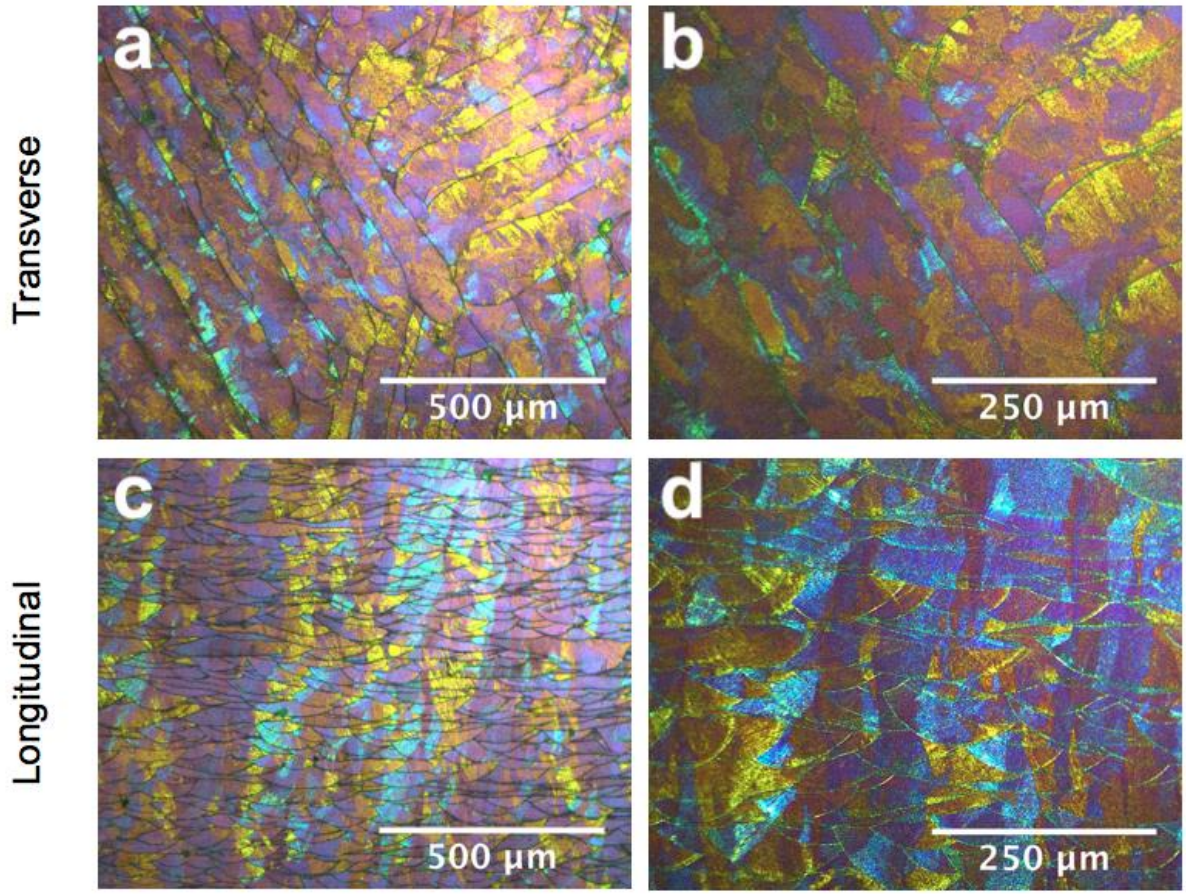

Figure 17: Optical micrographs in polarized light of a representative sample produced with LED higher than 150 J mm^{-3}: (a) low and (b) high magnification of transverse cross-section, (c) low and (d) high magnification longitudinal cross-section.

3.2.3 Micro-level microstructural features

At the micro-level all samples, regardless the LED value, exhibit the same microstructure, peculiar of the SLM technology and consequent to the extremely rapid solidification that leads to the formation of a metastable cellular microstructure [36]. Representative high magnification SEM micrographs are reported in Fig.18. In Fig.18a the previously discussed epitaxial grain growth

crossing over layers is evident: at least two growing directions can be clearly recognized, where elongated columnar grains can be identified. In the same image the collision between two growing directions is represented, as indicated by the white arrow in Fig.18a. It has indeed been reported [28,48] that grain growth is competitive and, when two different directions intercept, one of them might stop. The analyses revealed the presence, inside the solidified melt pools, of an extremely fine sub-micron cellular grain. These results are consistent with the outcomes reported by other authors for the same alloy processed via SLM [26–28,31]. Size and morphology of cellular grains can change between melt pools and even locally inside the same one: as represented in Fig.18b, cellular grains can be either almost circular or elongated, and grain size may vary from adjacent melt pools. Following the work done by Darvish et al. [50], an evaluation of the primary spacing of dendrites/cells (λ_1) was carried out on samples processed with low, medium and high LED, in order to verify if a correlation between the energy density and λ_1 exists. From this preliminary investigation it seems that the energy density does not exert a determinant influence on cells size; the average value measured in this experiment for λ_1 is 0.6 μm and it is consistent with literature data [50]. In addition, it is worth mentioning that very fine spherical porosities, with dimension lower than 1 μm, can be found in the microstructure, as highlighted by the white circle in Fig.18b. A SEM image at higher magnification of a melt pool boundary is reported In Fig.18c. According to the literature [26,27,30] a micro-level segregation between the core of cell grain and boundaries exists: center of the cell is rich in CoCr, while a higher concentration of Mo can be found at the grain boundaries. A number of SEM-EDS analyses were carried out in correspondence of track (melt pool) boundaries, with the aim to verify possible segregation, but no evidence of enrichment of any of the alloy elements was found. A possible explanation about the development of the cellular microstructure for the CoCrMo system during SLM was given by Prashanth and Eckert [36]. CoCrMo is a ternary diagram but, since the Mo content is too low for this alloy to form the ternary phase $Co_{49}Cr_{21}Mo_{30}$, CoCrMo system can be considered as a pseudo-binary diagram, with CoCr and Mo as the two phases. The low-melting CoCr phase directly forms from the liquid, ejecting the high-melting Mo phase, in account of the negligible

solubility of Mo in the CoCr phase, thus Mo is deposited on cellular boundaries. The formation of the cellular microstructure involves thermodynamic and kinetic theories, as well as physical aspects such as high thermal gradients and surface tension, that lead to the previously mentioned Marangoni convection flow that can cause solute accumulation [36]. The occurring of solute accumulation was also confirmed by Qian et al. [27] by reporting TEM analyses that revealed Cr and Mo enrichment in correspondence of cellular boundaries.

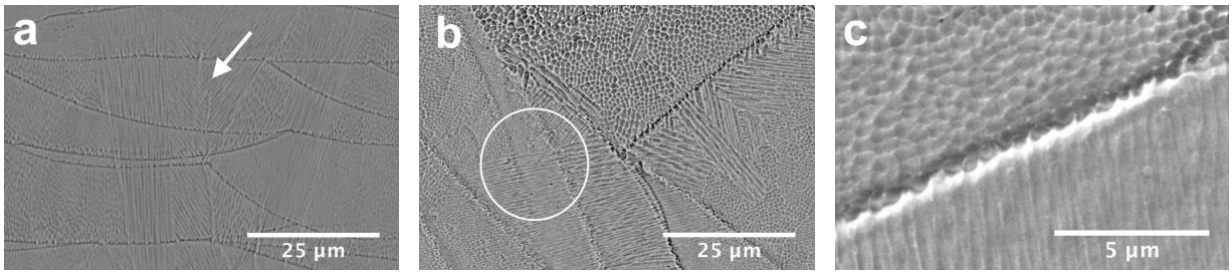

Figure 18: High magnification SEM micrographs of SLM parts cross-sections: the white arrow in a) indicates the intersection between two growing directions, the white circle in b) underlines sub-micro-sized porosities, c) magnification of a melt pool boundary.

SEM-EDS analyses were also performed on different areas of samples, processed with low, medium and high LED with the purpose to verify if chemical composition of final parts diverges from the one of the powders and if major vaporization of alloy elements occurs at high LED level. The results (Tab.4) showed that the average chemical composition complies with the requirements and no differences between samples or massive vaporization of elements were documented, even at high LED value.

Table 4: Average chemical composition (wt.%) measured by SEM-EDS on cross section of samples processed with low, medium and high LED.

	Co	Cr	Mo	Si	Mn
Low LED	62.6	28.9	6.6	0.9	1.0
Medium LED	62.5	28.8	6.9	0.9	1.0
High LED	62.6	28.8	6.8	0.9	0.9

Results of the X-ray diffraction analysis performed on longitudinal section of samples obtained at the three different level of LED are reported in Fig.19. The XRD spectra show that SLM samples mainly consist of γ (Co-fcc, ICDD:15-806) and ε (Co-hcp, ICDD:5-727) phases. At high LED value, the ε phase is slightly reduced in favor of the γ phase, while at low LED the two phases are almost equally present; this result suggests that different volume energies lead, as mentioned before, to different thermal gradients, thus facilitating or hindering the γ to ε transformation. Similar results were also reported by Molinari [61], for the same alloy produced by SLM under different process conditions.

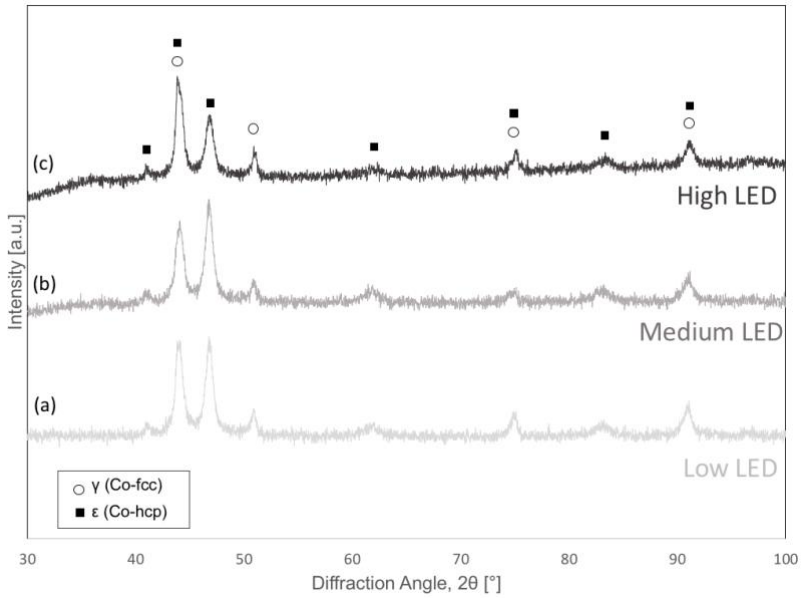

Figure 19: XRD analysis performed on representative SLM samples processed with: a) low LED, b) medium LED, c) high LED.

It is worth nothing that, according to the equilibrium phase diagram, the ε-hcp phase is stable at room temperature, while the γ-fcc phase is the high temperature stable phase (900-950°C). However, as also observed in conventional CoCr castings, since the transformation from fcc to hcp phase, occurring during cooling, is sluggish, usually the γ-fcc phase still exists at room temperature [62]. In addition, high cooling rates and small grain size (<100 μm), peculiar of the SLM technology, might

suppress the γ - ε transformation [26]. Due to the superposition of reflections of γ and ε phases, peaks approximately located at 2θ=44,75 and 92° correspond to both phases. For all samples, the highest intensity peaks were the ones located at about 2θ=44°, corresponding to γ(111) and ε(002), and at about 2θ=47.5°, corresponding to ε(101). This result confirmed a preferential crystal orientation, as reported in the literature and previously discussed in the present manuscript.

3.2.4 Hardness Measurements

Standard requirement for samples produced with conventional casting is 25-35 HRC in the as-cast condition [34]; HRC hardness was therefore evaluated on all the SLM samples and the results are reported, as a function of LED, in Fig. 20. As a result of the extremely fine microstructure, all samples, except for two, fulfill the standards, even in the case of low energy density, thus an elevated porosity content. Most of the samples exhibited even greater hardness, especially when their density was high (meaning LED>100 J mm^{-3}): samples of near-full-density presented an average hardness value of 36 ± 1 HRC.

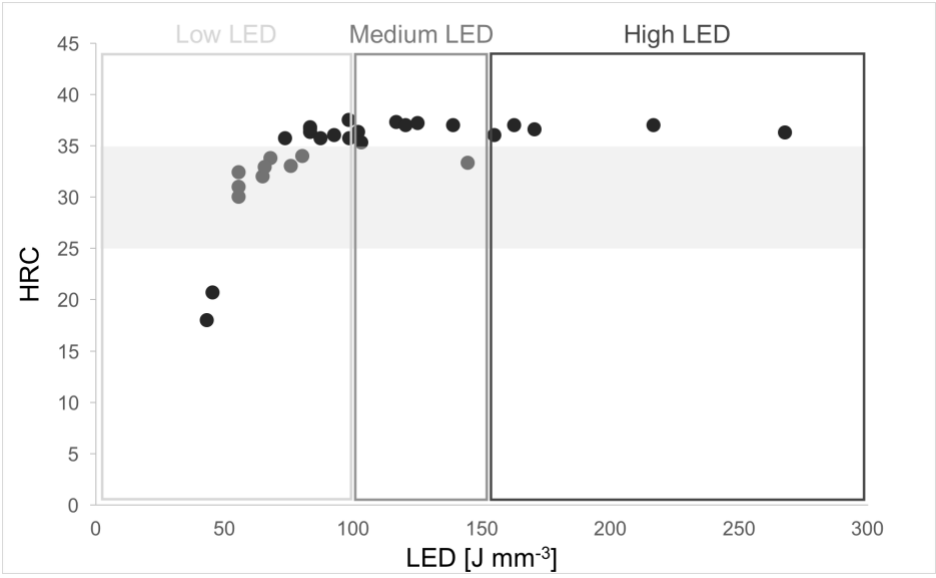

Figure 20: Hardness (HRC) of SLM samples as a function of LED. Grey band defines requirements given by ASTM F75 for a conventional cast component.

Eventually, microhardness measurements (HV0.5) were also performed on single melt pools, both on transverse and longitudinal cross sections, and the results are reported in Fig.21. So as for the micro-

level microstructure, the laser energy density does not seem to have a direct influence on microhardness of the SLM samples, since samples processed with very different LED returned a very similar microhardness. Average microhardness values lie in the range 380-430 HV0.5 and, for the majority of samples, transverse cross sections exhibit a lower hardness than the corresponding longitudinal ones, even if a high standard deviation was registered. These results might be ascribed to the intrinsic anisotropy that the SLM technology induces on the as built components, as a result of the strongly oriented columnar grain growth. Microhardness values are consistent with the ones reported for the Co-28Cr-6Mo alloy processed via SLM by Mergulhão et al. [31] and slightly lower than those measured by Qian et al. [27].

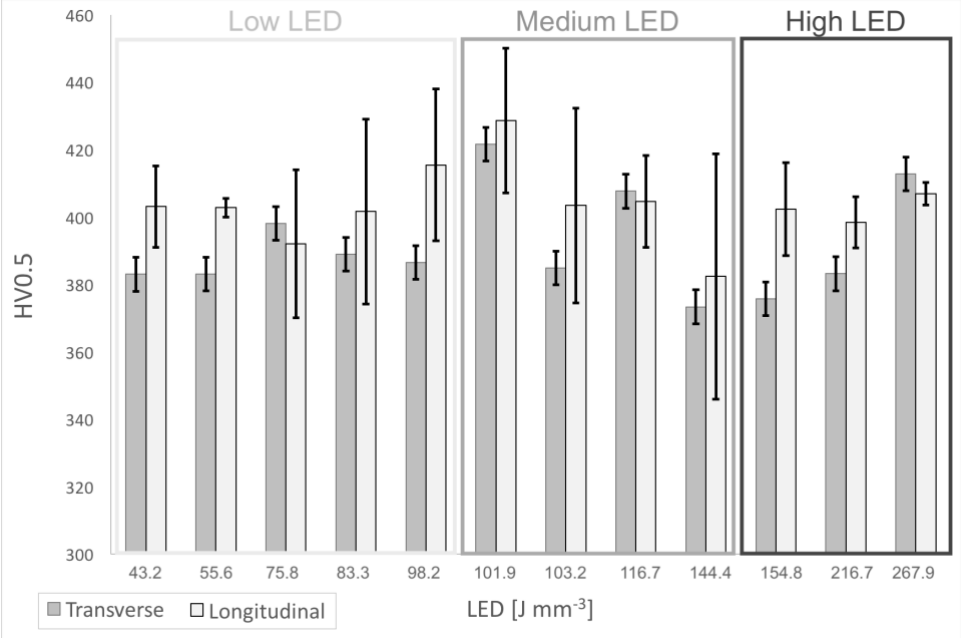

Figure 21: Average microhardness values (HV 0.5) measured both on longitudinal and transverse cross-sections of SLM samples processed with low, medium and high LED.

4. Conclusions

In the present work superface, microstructural and hardness properties of Co-28Cr-6Mo samples realized by SLM were analysed in-depth, with the aim to establish a correlation between the aforementioned properties and process parameters. A wide range of process parameters were considered, in order to explore a wide range of energy densities (LED=43.2 - 267.9 J mm^{-3}). Hence all outcomes have been related to three different classes of LED: low (up to 100 J mm^{-3}), medium (100-150 J mm^{-3}) and high (150-270 J mm^{-3}).

The following conclusion can be drawn:

- Low LED is not sufficient enough to fully melt the feedstock powders, thus the liquid pool is highly unstable. In account of extensive lacks of fusion, SLM samples exhibited a porosity content in the range 1-7 area%, high roughness on the top surface (Ra=13-7 μm) and a considerable variability in the macrohardness, ranging from 18 to 36 HRC.
- Medium and high LED succeeded in melting all powders and returned sound components, with a very low porosity content (0.5-0.1%) and smother top surfaces (Ra=5-2.5 μm); in addition, hardness values settled at 36 ± 1 HRC, with a very low variability. Dominant defects were micro-sized gas porosities although, if the energy density is to high (LED > 200 J mm^{-3}), keyhole collapses can occur.
- The energy density seems to have no direct effect on the quality of lateral surfaces of samples and on the laser tracks size, both on the transverse and longitudinal sections. In this view, further investigations might be conducted with the aim to identify influences of single process parameters. However, a promising roughness lower than 10 μm for lateral surfaces and lower than 4 μm for top surfaces, was obtained.
- At a micro-level scale, the microstructure of all samples exhibited similar features: cellular grains with epitaxial growth crossing over layers, oriented along the direction of the maximum heat gradient. Moreover, micro-hardness on single melt pools seems to have no direct correlation with LED values and measurements performed on transverse and longitudinal sections underlined a minor anisotropic behavior.

5. Acknowledgment

The authors would like to thanks Dr Erica Liverani and Dr Iuri Boromei at the University of Bologna for their precious contribution in samples production and SEM-EDS analyses. This research did not receive any specific grant from funding agencies in the public, commercial, or not-for-profit sectors. Declarations of interest: none.

References

[1] D.D. Gu, W. Meiners, K. Wissenbach, R. Poprawe, Laser additive manufacturing of metallic components: materials, processes and mechanisms, Int. Mater. Rev. 57 (2012) 133–164. doi:10.1179/1743280411Y.0000000014.

[2] W.E. Frazier, Metal additive manufacturing: A review, J. Mater. Eng. Perform. 23 (2014) 1917–1928. doi:10.1007/s11665-014-0958-z.

[3] C.Y. Yap, C.K. Chua, Z.L. Dong, Z.H. Liu, D.Q. Zhang, L.E. Loh, S.L. Sing, Review of selective laser melting: Materials and applications, Appl. Phys. Rev. 2 (2015) 041101-21. doi:10.1063/1.4935926.

[4] W.S.W. Harun, M.S.I.N. Kamariah, N. Muhamad, S.A.C. Ghani, F. Ahmad, Z. Mohamed, A review of powder additive manufacturing processes for metallic biomaterials, Powder Technol. 327 (2018) 128–151. doi:10.1016/j.powtec.2017.12.058.

[5] D. Herzog, V. Seyda, E. Wycisk, C. Emmelmann, Additive manufacturing of metals, Acta Mater. 117 (2016) 371–392. doi:10.1016/j.actamat.2016.07.019.

[6] T. DebRoy, H.L. Wei, J.S. Zuback, T. Mukherjee, J.W. Elmer, J.O. Milewski, A.M. Beese, A. Wilson-Heid, A. De, W. Zhang, Additive manufacturing of metallic components – Process, structure and properties, Prog. Mater. Sci. 92 (2018) 112–224. doi:10.1016/j.pmatsci.2017.10.001.

[7] T. De Terris, O. Andreau, P. Peyre, F. Adamski, I. Koutiri, C. Gorny, C. Dupuy, Optimization and comparison of porosity rate measurement methods of Selective Laser Melted metallic parts, Addit. Manuf. 28 (2019) 802–813. doi:10.1016/j.addma.2019.05.035.

[8] H. Materials, M. Guo, D. Gu, L. Xi, H. Zhang, J. Zhang, J. Yang, Selective laser melting additive manufacturing of pure tungsten : Role of volumetric energy density on densification, microstructure and mechanical properties, Int. J. Refract. Metals Hard Mater. 84 (2019) 105025. doi:10.1016/j.ijrmhm.2019.105025.

[9] Z.A. Mierrzejewska, Effect of Laser Energy Density, Internal Porosity and Heat Treatment on Mechanical Behavior of Biomedical Ti6Al4V Alloy Obtained with DMLS Technology, Materials (Basel). 12 (2019) 2331. doi:doi:10.3390/ma12142331.

[10] J.H. Yi, J.W. Kang, T.J. Wang, X. Wang, Y.Y. Hu, T. Feng, Y.L. Feng, P.Y. Wu, Effect of laser energy density on the microstructure, mechanical properties, and deformation of Inconel 718 samples

fabricated by selective laser melting, J. Alloys Compd. 786 (2019) 481–488. doi:10.1016/j.jallcom.2019.01.377.

[11] R. Casati, M. Coduri, N. Lecis, C. Andrianopoli, M. Vedani, Microstructure and mechanical behavior of hot-work tool steels processed by Selective Laser Melting, Mater. Charact. 137 (2018) 50–57. doi:10.1016/j.matchar.2018.01.015.

[12] R. Casati, J. Lemke, M. Vedani, Microstructure and Fracture Behavior of 316L Austenitic Stainless Steel Produced by Selective Laser Melting, J. Mater. Sci. Technol. 32 (2016) 738–744. doi:10.1016/j.jmst.2016.06.016.

[13] F. Hengsbach, P. Koppa, K. Duschik, M.J. Holzweissig, M. Burns, J. Nellesen, W. Tillmann, T. Tröster, K.P. Hoyer, M. Schaper, Duplex stainless steel fabricated by selective laser melting - Microstructural and mechanical properties, Mater. Des. 133 (2017) 136–142. doi:10.1016/j.matdes.2017.07.046.

[14] Y. Lu, S. Wu, Y. Gan, T. Huang, C. Yang, L. Junjie, J. Lin, Study on the microstructure, mechanical property and residual stress of SLM Inconel-718 alloy manufactured by differing island scanning strategy, Opt. Laser Technol. 75 (2015) 197–206. doi:10.1016/j.optlastec.2015.07.009.

[15] G. Marchese, X. Garmendia Colera, F. Calignano, M. Lorusso, S. Biamino, P. Minetola, D. Manfredi, Characterization and Comparison of Inconel 625 Processed by Selective Laser Melting and Laser Metal Deposition, Adv. Eng. Mater. 19 (2017) 1–9. doi:10.1002/adem.201600635.

[16] F. Caiazzo, V. Alfieri, G. Corrado, P. Argenio, Laser powder-bed fusion of Inconel 718 to manufacture turbine blades, Int. J. Adv. Manuf. Technol. 93 (2017) 4023–4031. doi:10.1007/s00170-017-0839-3.

[17] S. Marola, D. Manfredi, G. Fiore, M.G. Poletti, M. Lombardi, P. Fino, L. Battezzati, A comparison of Selective Laser Melting with bulk rapid solidification of AlSi10Mg alloy, J. Alloys Compd. 742 (2018) 271–279. doi:10.1016/j.jallcom.2018.01.309.

[18] F. Trevisan, F. Calignano, M. Lorusso, J. Pakkanen, A. Aversa, E.P. Ambrosio, M. Lombardi, P. Fino, D. Manfredi, On the selective laser melting (SLM) of the AlSi10Mg alloy: Process, microstructure, and mechanical properties, Materials (Basel). 10 (2017). doi:10.3390/ma10010076.

[19] E.O. Olakanmi, R.F. Cochrane, K.W. Dalgarno, A review on selective laser sintering/melting (SLS/SLM) of aluminium alloy powders: Processing, microstructure, and properties, Prog. Mater. Sci. 74 (2015) 401–477. doi:10.1016/j.pmatsci.2015.03.002.

[20] C.A. Biffi, J. Fiocchi, A. Tuissi, Selective laser melting of AlSi10 Mg: Influence of process parameters on Mg2Si precipitation and Si spheroidization, J. Alloys Compd. 755 (2018) 100–107. doi:10.1016/j.jallcom.2018.04.298.

[21] S. Bose, D. Ke, H. Sahasrabudhe, A. Bandyopadhyay, Additive manufacturing of biomaterials, Prog. Mater. Sci. 93 (2018) 45–111. doi:10.1016/j.pmatsci.2017.08.003.

[22] L. Kunčická, R. Kocich, T.C. Lowe, Advances in metals and alloys for joint replacement, Prog. Mater. Sci. 88 (2017) 232–280. doi:10.1016/j.pmatsci.2017.04.002.

[23] T. Ozel, P. Bartolo, E. Ceretti, J. De Ciurana Gay, C.A. Rodriguez, J.V.L. Da Silva, Biomedical Devices: Design, Prototyping and Manufacturing, John Wiley & Sons, 2017.

doi:10.1002/9781119267034.

[24] Q. Chen, G.A. Thouas, Metallic implant biomaterials, Mater. Sci. Eng. R Reports. 87 (2015) 1–57. doi:10.1016/j.mser.2014.10.001.

[25] G. Mani, Metallic Biomaterials: Cobalt-Chromium Alloys, in: W. Murphy, J. Black, G. Hastings (Eds.), Handb. Biomater. Prop., Second Edi, Springer, 2016: pp. 159–166.

[26] A. Takaichi, Suyalatu, T. Nakamoto, N. Joko, N. Nomura, Y. Tsutsumi, S. Migita, H. Doi, S. Kurosu, A. Chiba, N. Wakabayashi, Y. Igarashi, T. Hanawa, Microstructures and mechanical properties of Co-29Cr-6Mo alloy fabricated by selective laser melting process for dental applications, J. Mech. Behav. Biomed. Mater. 21 (2013) 67–76. doi:10.1016/j.jmbbm.2013.01.021.

[27] B. Qian, K. Saeidi, L. Kvetková, F. Lofaj, C. Xiao, Z. Shen, Defects-tolerant Co-Cr-Mo dental alloys prepared by selective laser melting, Dent. Mater. 31 (2015) 1435–1444. doi:10.1016/j.dental.2015.09.003.

[28] Z.W. Chen, M.A.L. Phan, K. Darvish, Grain growth during selective laser melting of a Co–Cr–Mo alloy, J. Mater. Sci. 52 (2017) 7415–7427. doi:10.1007/s10853-017-0975-z.

[29] E. Liverani, A. Fortunato, A. Leardini, C. Belvedere, S. Siegler, L. Ceschini, A. Ascari, Fabrication of Co-Cr-Mo endoprosthetic ankle devices by means of Selective Laser Melting (SLM), Mater. Des. 106 (2016) 60–68. doi:10.1016/j.matdes.2016.05.083.

[30] M. Seyedi, F. Zanotto, C. Monticelli, A. Balbo, E. Liverani, A. Fortunato, Microstructural characterization and corrosion behaviour of SLM CoCrMo alloy in simulated body fluid, Metall. Ital. 110 (2018) 45–50.

[31] M.V. Mergulhão, C.E. Podestá, M.D.M. das Neves, Valuation of Mechanical Properties and Microstructural Characterization of ASTM F75 Co-Cr Alloy Obtained by Selective Laser Melting (SLM) and Casting Techniques, Mater. Sci. Forum. 899 (2017) 323–328. doi:10.4028/www.scientific.net/MSF.899.323.

[32] C. Song, M. Zhang, Y. Yang, D. Wang, Y. Jia-kuo, Morphology and properties of CoCrMo parts fabricated by selective laser melting, Mater. Sci. Eng. A. 713 (2018) 206–213. doi:10.1016/j.msea.2017.12.035.

[33] C. Song, Y. Yang, Y. Wang, D. Wang, J. Yu, Research on rapid manufacturing of CoCrMo alloy femoral component based on selective laser melting, Int. J. Adv. Manuf. Technol. 75 (2014) 445–453. doi:10.1007/s00170-014-6150-7.

[34] ASTM F75-12 Standard Specification for Cobalt-28 Chromium-6 Molybdenum Alloy Castings and Casting Alloy for Surgical Implants (UNS R30075), (2012). doi:https://doi.org/10.1520/F0075-12.

[35] G.F. Vander Voort, ASM Handbook Volume 9 - Metallography and Microstructures, ASM Interbational, 2004. doi:https://doi.org/10.31399/asm.hb.v09.9781627081771.

[36] K.G. Prashanth, J. Eckert, Formation of metastable cellular microstructures in selective laser melted alloys, J. Alloys Compd. 707 (2017) 27–34. doi:10.1016/j.jallcom.2016.12.209.

[37] R.J. Hebert, Viewpoint: metallurgical aspects of powder bed metal additive manufacturing, J. Mater.

Sci. 51 (2016) 1165–1175. doi:10.1007/s10853-015-9479-x.

[38] W.J. Sames, F.A. List, S. Pannala, R.R. Dehoff, S.S. Babu, The metallurgy and processing science of metal additive manufacturing, Int. Mater. Rev. 6608 (2016) 1–46. doi:10.1080/09506608.2015.1116649.

[39] J.A. Slotwinski, E.J. Garboczi, K.M. Hebenstreit, Porosity Measurements and Analysis for Metal Additive Manufacturing Process Control, J. Res. Natl. Inst. Stand. Technol. 119 (2014) 494–528. doi:10.6028/jres.119.019.

[40] A. Townsend, N. Senin, L. Blunt, R.K. Leach, J.S. Taylor, Surface texture metrology for metal additive manufacturing: a review, Precis. Eng. 46 (2016) 34–47. doi:10.1016/j.precisioneng.2016.06.001.

[41] X. Zhou, K. Li, D. Zhang, X. Liu, J. Ma, W. Liu, Z. Shen, Textures formed in a CoCrMo alloy by selective laser melting, J. Alloys Compd. 631 (2015) 153–164. doi:10.1016/j.jallcom.2015.01.096.

[42] X. Zhou, X. Liu, D. Zhang, Z. Shen, W. Liu, Balling phenomena in selective laser melted tungsten, J. Mater. Process. Technol. 222 (2015) 33–42. doi:10.1016/j.jmatprotec.2015.02.032.

[43] C. Qiu, C. Panwisawas, M. Ward, H.C. Basoalto, J.W. Brooks, M.M. Attallah, On the role of melt flow into the surface structure and porosity development during selective laser melting, Acta Mater. 96 (2015) 72–79. doi:10.1016/j.actamat.2015.06.004.

[44] D. Wang, S. Wu, F. Fu, S. Mai, Y. Yang, Y. Liu, C. Song, Mechanisms and characteristics of spatter generation in SLM processing and its effect on the properties, Mater. Des. 117 (2017) 121–130. doi:10.1016/j.matdes.2016.12.060.

[45] C. Zhao, K. Fezzaa, R.W. Cunningham, H. Wen, F. De Carlo, L. Chen, A.D. Rollett, T. Sun, Real-time monitoring of laser powder bed fusion process using high-speed X-ray imaging and diffraction, Sci. Rep. 7 (2017) 1–11. doi:10.1038/s41598-017-03761-2.

[46] P. Bidare, I. Bitharas, R.M. Ward, M.M. Attallah, A.J. Moore, Fluid and particle dynamics in laser powder bed fusion, Acta Mater. 142 (2018) 107–120. doi:10.1016/j.actamat.2017.09.051.

[47] M.J. Matthews, G. Guss, S.A. Khairallah, A.M. Rubenchik, P.J. Depond, W.E. King, Denudation of metal powder layers in laser powder bed fusion processes, Acta Mater. 114 (2016) 33–42. doi:10.1016/j.actamat.2016.05.017.

[48] P.C. Collins, D.A. Brice, P. Samimi, I. Ghamarian, H.L. Fraser, Microstructural Control of Additively Manufactured Metallic Materials, Annu. Rev. Mater. Res. 46 (2016) 63–91. doi:10.1146/annurev-matsci-070115-031816.

[49] ASTM E112 - 13 - Standard Test Methods for Determining Average Grain Size, (2013). doi:10.1520/E0112.

[50] K. Darvish, Z.W. Chen, M.A.L. Phan, T. Pasang, Selective laser melting of Co-29Cr-6Mo alloy with laser power 180–360 W: Cellular growth, intercellular spacing and the related thermal condition, Mater. Charact. 135 (2018) 183–191. doi:10.1016/j.matchar.2017.11.042.

[51] B. Zhang, Y. Li, Q. Bai, Defect Formation Mechanisms in Selective Laser Melting: A Review, Chinese J. Mech. Eng. 30 (2017) 515–527. doi:10.1007/s10033-017-0121-5.

[52] R. Rai, J.W. Elmer, T.A. Palmer, T. DebRoy, Heat transfer and fluid flow during keyhole mode laser welding of tantalum, Ti–6Al–4V, 304L stainless steel and vanadium, J. Phys. D. Appl. Phys. 40 (2007) 5753–5766. doi:10.1088/0022-3727/40/18/037.

[53] W.E. King, H.D. Barth, V.M. Castillo, G.F. Gallegos, J.W. Gibbs, D.E. Hahn, C. Kamath, A.M. Rubenchik, Observation of keyhole-mode laser melting in laser powder-bed fusion additive manufacturing, J. Mater. Process. Technol. 214 (2014) 2915–2925. doi:10.1016/j.jmatprotec.2014.06.005.

[54] V.-P. Matilainen, H. Piili, A. Salminen, O. Nyrhilä, Preliminary Investigation of Keyhole Phenomena during Single Layer Fabrication in Laser Additive Manufacturing of Stainless Steel, Phys. Procedia. 78 (2015) 377–387. doi:10.1016/j.phpro.2015.11.052.

[55] I. Rosenthal, A. Stern, N. Frage, Strain rate sensitivity and fracture mechanism of AlSi10Mg parts produced by Selective Laser Melting, Mater. Sci. Eng. A. 682 (2017) 509–517. doi:10.1016/j.msea.2016.11.070.

[56] J. V. Giacchi, C.N. Morando, O. Fornaro, H.A. Palacio, Microstructural characterization of as-cast biocompatible Co-Cr-Mo alloys, Mater. Charact. 62 (2011) 53–61. doi:10.1016/j.matchar.2010.10.011.

[57] H.R. Kim, S.H. Jang, Y.K. Kim, J.S. Son, B.K. Min, K.H. Kim, T.Y. Kwon, Microstructures and mechanical properties of Co-Cr dental alloys fabricated by three CAD/CAM-based processing techniques, Materials (Basel). 9 (2016). doi:10.3390/MA9070596.

[58] S. Dadbakhsh, B. Vrancken, J.P. Kruth, J. Luyten, J. Van Humbeeck, Texture and anisotropy in selective laser melting of NiTi alloy, Mater. Sci. Eng. A. 650 (2016) 225–232. doi:10.1016/j.msea.2015.10.032.

[59] L. Thijs, K. Kempen, J.P. Kruth, J. Van Humbeeck, Fine-structured aluminium products with controllable texture by selective laser melting of pre-alloyed AlSi10Mg powder, Acta Mater. 61 (2013) 1809–1819. doi:10.1016/j.actamat.2012.11.052.

[60] L. Thijs, M.L. Montero Sistiaga, R. Wauthle, Q. Xie, J.P. Kruth, J. Van Humbeeck, Strong morphological and crystallographic texture and resulting yield strength anisotropy in selective laser melted tantalum, Acta Mater. 61 (2013) 4657–4668. doi:10.1016/j.actamat.2013.04.036.

[61] A. Molinari, The structural metastability of metallic alloys produced by Selective Laser Melting, La Metall. Ital. 1 (2017) 21–27.

[62] R. Narayan, ASM Handbook, Volume 23, Materials for Medical Devices, ASM International, 2012.